Distinct Activation Mechanisms of CXCR4 and ACKR3 Revealed by Single-Molecule Analysis of their Conformational Landscapes

Christopher T. Schafer[a,1], Raymond F. Pauszek III[b,2], Martin Gustavsson[a,3], Tracy M. Handel[a]*, and David P. Millar[b]*

[a] Skaggs School of Pharmacy and Pharmaceutical Sciences, Department of Pharmacology, University of California San Diego, La Jolla, CA 92037.
[b] Department of Integrative Structural and Computational Biology, The Scripps Research Institute, La Jolla, CA 92037.
[1] Present address: Amsterdam Institute for Molecular and Life Sciences, Department of Medicinal Chemistry, Faculty of Science, Vrije Universiteit Amsterdam, 1081 HV Amsterdam, Netherlands
[2] Present address: LUMICKS, 1105 AG Amsterdam, Netherlands
[3] Present address: Department of Biomedical Sciences, Faculty of Health and Medical Sciences, University of Copenhagen, 2200 Copenhagen, Denmark

*Correspondence and requests for materials should be addressed to D.P.M. (millar@scripps.edu) or T.M.H. (thandel@health.ucsd.edu)

Keywords: Chemokine receptor, single-molecule FRET, GPCR, ACKR3, conformational dynamics

This PDF file includes:

Main Text
Figures 1 to 6

Abstract

The canonical chemokine receptor CXCR4 and atypical receptor ACKR3 both respond to CXCL12 but induce different effector responses to regulate cell migration. While CXCR4 couples to G proteins and directly promotes cell migration, ACKR3 is G protein-independent and scavenges CXCL12 to regulate extracellular chemokine levels and maintain CXCR4 responsiveness, thereby indirectly influencing migration. The receptors also have distinct activation requirements. CXCR4 only responds to wild-type CXCL12 and is sensitive to mutation of the chemokine. By contrast, ACKR3 recruits GPCR kinases (GRKs) and β-arrestins and promiscuously responds to CXCL12, CXCL12 variants, other peptides and proteins, and is relatively insensitive to mutation. To investigate the role of conformational dynamics in the distinct pharmacological behaviors of CXCR4 and ACKR3, we employed single-molecule FRET to track discrete conformational states of the receptors in real-time. The data revealed that apo-CXCR4 preferentially populates a high-FRET inactive state, while apo-ACKR3 shows little conformational preference and high transition probabilities among multiple inactive, intermediate and active conformations, consistent with its propensity for activation. Multiple active-like ACKR3 conformations are populated in response to agonists, compared to the single CXCR4 active-state. This and the markedly different conformational landscapes of the receptors suggest that activation of ACKR3 may be achieved by a broader distribution of conformational states than CXCR4. Much of the conformational heterogeneity of ACKR3 is linked to a single residue that differs between ACKR3 and CXCR4. The dynamic properties of ACKR3 may underly its inability to form productive interactions with G proteins that would drive canonical GPCR signaling.

Main Text

Introduction

CXC chemokine receptor 4 (CXCR4) is one of the most intensively studied chemokine receptors due to its central role in driving cell migration during development and immune responses, and in cancer where it promotes tumor growth and metastasis (1-4). As a class A G protein-coupled receptor (GPCR), CXCR4 activates inhibitory Gαi protein signaling pathways to directly control cell movement in response to the chemokine CXCL12 (5). The activated receptor is also phosphorylated by GPCR kinases (GRKs), which promotes arrestin recruitment and cessation of the G protein signal. CXCR4 often works together with atypical chemokine receptor 3 (ACKR3, formerly CXCR7) which indirectly influences migration by scavenging CXCL12 to regulate available extracellular levels of the agonist and in turn the responsiveness of CXCR4 (6-8). In the absence of ACKR3 scavenging, excessive CXCL12 stimulation of CXCR4 leads to downregulation, resulting in profound effects on neuronal cell migration and development (9-11).

In contrast to CXCR4 and with some exceptions noted (12, 13), ACKR3 lacks G protein activity and instead is considered to be arrestin-biased (14). However, we and others (9) have shown that arrestins are dispensable for chemokine scavenging while GRK phosphorylation is critical for this function (15), suggesting that ACKR3 might be better described as GRK-biased. The molecular basis for its inability to couple to G proteins in most cell types remains an unanswered question. Our recently determined structures of ACKR3-ligand complexes showed the expected hallmarks of GPCR activation including "microswitch residues" in active state configurations, displacement of transmembrane helix 6 (TM6) away from the helical bundle and an open intracellular pocket, consistent with a receptor that should be able to activate G proteins (16). Accordingly, we replaced the intracellular loops (ICLs) of ACKR3 with those of CXCR2, a canonical G protein-coupled chemokine receptor; however, these changes did not lead to G protein activation (16), suggesting that the lack of coupling is not due to the absence of specific residue interactions. CXCL12 also adopts a distinct pose when bound to ACKR3 compared to CXCR4 and all other chemokines in chemokine-receptor complexes, but since small molecules induce similar biased effector responses, the chemokine pose cannot explain the effector-coupling bias (16). Having excluded other mechanisms we therefore surmised that the inability of ACKR3 to activate G proteins may be due to differences in receptor dynamics. Consistent with this hypothesis, the ICLs observed in ACKR3-agonist complexes are disordered, which may preclude productive effector coupling. The dynamic nature of ACKR3 is also suggested by its considerable constitutive activity in recruiting β-arrestins and its high level of constitutive internalization (16-18).

In addition to their distinct effector interactions, ACKR3 and CXCR4 have dramatically different susceptibilities to activation by different ligands. CXCR4 is activated by a single chemokine agonist, CXCL12. Moreover, modifications of the CXCL12 N-terminal signaling domain (e.g. single point mutations as in $CXCL12_{P2G}$ or multiple mutations as in $CXCL12_{LRHQ}$) transform the chemokine into an antagonist of CXCR4 (19, 20). Mutational analysis, modeling, and new structures of CXCR4 suggest that ligand activation involves a precise network of interacting residues that stabilize the active receptor conformation (21-25). By contrast, ACKR3 is activated by CXCL12 as well as its variants (including $CXCL12_{P2G}$ and $CXCL12_{LRHQ}$ (19, 20)), other chemokines (CXCL11) (26), other proteins (adrenomedullin, BAM22) (27, 28), and opioid peptides (29). In fact, most ligands for ACKR3 act as agonists, which is best explained by a non-specific "distortion" mechanism

of activation whereby any ligand that breaches the binding pocket causes helical movements that are permissive to GRK phosphorylation and arrestin recruitment. A distortion mechanism is consistent with the different binding poses observed for a small molecule agonist compared to the CXCL12 N-terminus in the receptor orthosteric pocket (16), and ligand bulk rather than specific interactions between agonist and ACKR3 being required for activation. We hypothesize that this distortion mechanism would also be facilitated by a receptor that is conformationally dynamic, by enabling nonspecific ligand interactions and more than a single conformation to promote activation.

To investigate the role of conformational dynamics in the distinct pharmacological behaviors of ACKR3 and CXCR4, we developed a single-molecule Förster resonance energy transfer (smFRET) approach. Many ensemble methods such as EPR, NMR and fluorescence-based methods have provided considerable insights into GPCR dynamics, conformational heterogeneity, and exchange between distinct structural states (30-36). However, these methods are limited in their ability to resolve the sequence of state-to-state transitions except in rare cases where transitions can be temporally coordinated with high precision (37). By contrast smFRET enables detection of sparsely populated states, reveals the sequence of state-to-state transitions and provides kinetic information through analysis of state dwell times. For example, smFRET studies of the β_2 adrenergic receptor (β_2AR) revealed a dynamic equilibrium between inactive and active conformations that was responsive to agonist and G protein binding (38). More recent smFRET studies of the glucagon receptor (39) and the A_{2A} receptor (A_{2A}R) (40) have documented the existence of distinct intermediate conformations in addition to inactive and active receptor conformations.

Here we present the first smFRET study of the chemokine receptors CXCR4 and ACKR3. Our experimental system allows real-time observation of the conformational fluctuations of individual receptor molecules in a native-like lipid environment and assessment of the differences in the conformational dynamics of the two receptors in their apo states and in response to ligands. Our results indicate that ACKR3 is more dynamic and conformationally heterogeneous than CXCR4 or other class A GPCRs previously studied, which may explain its activation prone nature and lack of G protein coupling. In contrast, CXCR4 appears less flexible, consistent with a more restricted, structurally-defined activation mechanism. Together these data characterize the molecular differences between CXCR4 and ACKR3 and suggest that enhanced conformational dynamics plays an important role in the atypical function of ACKR3.

Results

<u>Development of smFRET experimental systems for CXCR4 and ACKR3.</u>

To visualize conformational fluctuations of CXCR4 and ACKR3 by smFRET, cysteine residues were introduced into CXCR4 at positions $150^{4.40}$ in TM4 and $233^{6.29}$ in TM6, and at $159^{4.40}$ and $245^{6.28}$ in ACKR3 (Figs. S1A & B) (numbers in superscript refer to the Ballesteros-Weinstein numbering scheme for GPCRs) for covalent labeling with FRET donor (D, Alexa Fluor 555, A555) and acceptor (A, Cyanine5, Cy5) fluorophores. Single receptor molecules of labeled CXCR4 or ACKR3 were reconstituted into phospholipid nanodiscs to mimic the native membrane bilayer environment. Nanodiscs have been used in a wide variety of structural and biophysical studies of integral membrane proteins, including ACKR3, and reconstitute protein-lipid interactions lost in detergent systems (41-43). The nanodisc-receptor complexes were then tethered to a quartz slide through

150 biotinylation of the nanodisc membrane scaffolding protein (MSP) (Fig. 1A). To promote
151 monomeric receptor incorporation in each nanodisc, we utilized MSP1E3D1, which forms
152 nanodiscs with a diameter of approximately 13 nm (44, 45).
153
154 Crystal and cryo-electron microscopy (cryo-EM) structures of homologous class A
155 GPCRs, such as β_2AR, in inactive and active conformations, reveal that TM6 moves
156 outwards from the TM helical bundle during activation, whereas the position of TM4
157 remains relatively fixed (46). Accordingly, we anticipated that labeling at the positions
158 indicated above would be sensitive to transitions between inactive and active receptor
159 conformations and would give rise to different donor-acceptor distances and apparent
160 FRET efficiencies that could be resolved by smFRET measurements (shown
161 schematically in Fig. 1B). These positions are similar to those used effectively for β_2AR
162 (38), A_{2A}R, (40), and the μ-opioid receptor (47) for monitoring their conformational
163 dynamics by smFRET. Importantly, neither wild-type (WT) CXCR4 nor ACKR3 exhibited
164 significant labeling, obviating the need to remove any of the native cysteine residues in
165 either receptor. Moreover, the double cysteine receptor mutants retained CXCL12-
166 promoted β-arrestin2 recruitment (Figs. S1C & D). Only the E_{max} for arrestin recruitment
167 to CXCL12-stimulated ACKR3 was significantly altered by the mutations, while all other
168 pharmacological parameters were the same as for WT receptors.
169
170 <u>ACKR3 exhibits greater conformational dynamics than CXCR4.</u>
171 Receptor-nanodisc complexes were imaged on the slide surface using smFRET
172 microscopy by exciting the A555 donor with a green (532 nm) laser and monitoring the
173 resulting emission from both A555 and the Cy5 acceptor over time on separate segments
174 of a CCD camera. Several hundred individual receptor-nanodisc complexes were typically
175 observed in the field of view. Individual receptor molecules labeled with a single A555
176 donor and a single Cy5 acceptor were identified by single-step photobleaching transitions
177 (abrupt loss of acceptor fluorescence signal or simultaneous loss of fluorescence signal
178 in both channels), as shown for two representative ACKR3-nanodisc complexes in Fig.
179 1C. Additionally, anti-correlated changes in donor and acceptor emission prior to
180 photobleaching confirmed that FRET occurred between A555 and Cy5. Additional
181 examples of single-molecule traces for ACKR3 and CXCR4 are shown in Fig. S2. Dwell
182 times spent in one FRET level prior to switching to another level are generally in the
183 seconds range (Figs. 1C & S2).
184
185 The apparent FRET efficiencies from many individual receptor-nanodisc complexes,
186 recorded in the presence or absence of different ligands, were globally analyzed using
187 Hidden Markov Models (HMMs) assuming the presence of two, three, four, or five FRET
188 states (Materials and Methods). To evaluate the appropriate level of model complexity,
189 each resulting apparent FRET efficiency distribution was fit with a Gaussian Mixture Model
190 (GMM) and the corresponding Bayesian Information Criterion (BIC) was calculated. The
191 BIC is a statistical measure of the likelihood that the model describes the data, while also
192 penalizing the addition of parameters that could lead to overfitting of noise. Theoretically,
193 this value will be at a minimum for the model with the appropriate number of states. As an
194 additional criterion, we carefully compared the FRET distributions following the initial HMM
195 analysis for the different models and confirmed that peak positions were consistent across
196 the different experimental conditions.
197

These analyses indicated that three FRET states were sufficient to fit the smFRET data for CXCR4 under all conditions (Figs. S3 & S4). The resulting apparent FRET efficiency distributions are presented in Figs. 2A & B. The predominant high-FRET state (E_{app} = 0.85) observed in the apo-state (Fig. 2A) suggests that TM4 and 6 are in close physical proximity, which is consistent with the conformation of inactive GPCRs (48, 49). Accordingly, we interpret this FRET state as the inactive conformation of CXCR4 and designate it as R. The minor low-FRET state (E_{app} = 0.19) reflects outward movement of TM6 away from TM4, as expected for an active receptor conformation (designated R*) (46, 50) and consistent with the limited basal activity of CXCR4. Moreover, there was a major population shift from the high-FRET state to the low-FRET state upon addition of $CXCL12_{WT}$ (Fig. 2B), consistent with the expected stabilization of active GPCR conformations by agonists (51, 52). To gain insight into the nature of the mid-FRET state (E_{app} = 0.59), we examined the connectivity between all three FRET states. Two-dimensional transition density probability (TDP) plots revealed that the three FRET states were connected in a sequential fashion (Figs. 2A & B), indicating that the transitions occurred within the same molecules. Notably, these observations exclude the possibility that the mid-FRET state arises from different local fluorophore environments (hence FRET efficiencies) for the two possible labeling orientations of the introduced cysteines: assuming two receptor conformations, this model would produce four distinct FRET states, but only two cross peaks in the TDP plot. Another significant observation is that direct transitions between R and R* states were rarely observed (Figs. 2A & B). Taken together, these results suggest that the mid-FRET state represents an intermediate receptor conformation (designated R') that lies on the pathway between inactive and active conformations. In the apo-state, transitions were mostly observed between states R and R' (Fig. 2A), while in the presence of $CXCL12_{WT}$ the most frequent transitions were observed between the R' and R* states (Fig. 2B).

In contrast, the apparent FRET efficiency histogram for ACKR3 in the apo state (Fig. 2C) was much broader than the corresponding histogram for CXCR4 (Fig. 2A), indicating greater conformational heterogeneity. Moreover, the smFRET data for ACKR3 could not be described by three FRET states and the inclusion of a fourth state was necessary (Figs. S5 & S6). The FRET distributions recovered by four-state global analysis are presented in Figs. 2C & D. The positions of the high-FRET (E_{app} = 0.85) and low-FRET (E_{app} = 0.11) peaks are similar to the corresponding peaks observed in CXCR4 and are likewise assigned to inactive (R) and active (R*) conformations, respectively. Consistent with these assignments, the R* state increased in population at the expense of the R state in the presence of the chemokine agonists $CXCL12_{WT}$ (Fig. 2D) or CXCL11 (Fig. S7B). TDP plots indicated that the four FRET states in ACKR3 were connected in a sequential fashion and reside along the receptor activation pathway (Figs. 2C & D). Similar to the arguments presented above for CXCR4, the intermediate FRET states are most likely discrete receptor conformations and not arising from mixed labeling of the two introduced cysteines. Accordingly, the mid-FRET peaks (E_{app} = 0.39 and E_{app} = 0.66) are assigned to two intermediate receptor conformations, designated R*' and R', respectively. Notably, the R*' state was not observed in CXCR4 (Figs. 2A & B). The R' state in ACKR3 decreased in population in the presence of chemokine agonists (Fig. 2D, Fig. S7B), suggesting that this state represents an inactive intermediate receptor conformation, consistent with its position on the conformational pathway (closest to R). In striking contrast to apo-CXCR4, apo-ACKR3 populated the four conformational states more or less equally, and all possible sequential conformational transitions were observed (Fig. 2C). Thus, ACKR3 is

247 intrinsically more conformationally heterogenous and dynamic than CXCR4. In the
248 presence of $CXCL12_{WT}$, ACKR3 showed more frequent R' ↔ R*' and R*' ↔ R* transitions
249 compared with the apo-receptor, accounting for the population shift towards the R* state
250 (Figs. 2C & D).
251
252 Effect of small-molecule ligands on conformational states of CXCR4 and ACKR3.
253 The small-molecule ligand IT1t is reported to act as an inverse agonist of CXCR4 (53-55).
254 However, the conformational distribution of CXCR4 showed little change to the overall
255 apparent FRET profile, although R' ↔ R* transitions appeared in the TDP plot (Figs. 3A
256 & B, Fig. S8). This suggests that the small molecule does not suppress CXCR4 basal
257 signaling by changing the conformational equilibrium. Instead IT1t appears to increase
258 transition probabilities which may impair G protein coupling by CXCR4.
259
260 Treatment of ACKR3 with the small-molecule agonist VUF15485 (56) shifted the
261 conformational distribution of the receptor towards the active R* state (Figs. S7C & S8),
262 as expected for an agonist and supporting the assignment of the R* FRET state. In
263 contrast, treatment of ACKR3 with the small-molecule inverse agonist VUF16840 (52)
264 shifted the conformational distribution to the inactive R conformation, with a concomitant
265 decrease of R* (Fig. 3D, Fig. S8), consistent with the expected effect of an inverse agonist
266 and with suppression of the basal activity of ACKR3 by this ligand (52). The intermediate
267 R*' population also decreased in the presence of the inverse agonist (Fig. 3D, Fig. S8),
268 suggesting that this state represents an active-like receptor conformation, consistent with
269 its placement on the conformational pathway (closest to R*). The suppression of active
270 receptor conformations was also evident in the TDP, which revealed fewer transitions
271 between R*' and R* conformations relative to the apo receptor (Figs. 3C & D).
272
273 CXCL12 N-terminal mutants promote active receptor conformations despite their
274 contrasting pharmacological effects on CXCR4 and ACKR3.
275 CXCR4 is sensitive to N-terminal mutations of CXCL12 while ACKR3 is relatively
276 insensitive. For example, the variant $CXCL12_{P2G}$, containing a proline to glycine mutation
277 in the second position, and $CXCL12_{LRHQ}$, where the first three residues of $CXCL12_{WT}$ are
278 replaced with the four-residue motif LRHQ starting with L0, are antagonists of CXCR4 but
279 agonists of ACKR3 (19, 20). To gain further insight into the ligand-dependent responses
280 of CXCR4 and ACKR3, we examined how these mutant chemokines influence the
281 conformational states and dynamics of both receptors.
282
283 Surprisingly, $CXCL12_{P2G}$ promoted a shift to the active R* conformation of CXCR4
284 compared to the apo-receptor (R* increased by 16%, Figs. 4A & B, Fig. S8), although the
285 shift was less pronounced than observed for $CXCL12_{WT}$ (28% increase in R*, Fig. 2B, Fig.
286 S8). The shift is also evident in the TDPs where the state-to-state transitions involving the
287 R* active state were more probable for the $CXCL12_{P2G}$ complex compared with apo-
288 CXCR4 (Figs. 4A & B). The presence of $CXCL12_{LRHQ}$ had a more subtle effect on CXCR4:
289 the active R* conformation increased by 9% (Figs. 4A & C, Fig. S8). Despite the ability of
290 $CXCL12_{P2G}$ and $CXCL12_{LRHQ}$ to stabilize the active R* conformation of CXCR4, both
291 variants are known to act as antagonists (20). This suggests that the CXCL12 mutants
292 inhibit CXCR4 coupling to G proteins not by suppressing the active receptor population
293 but rather by increasing the dynamics of the receptor state-to-state transitions. Our results
294 suggest that the helical movements considered classic signatures of the active state may
295 not be sufficient for CXCR4 to engage productively with G proteins..

In the case of ACKR3, $CXCL12_{P2G}$ induced a modest increase in the population of the active R* conformation relative to the apo-receptor (R* increased by 5%, Figs. 4D & E, Fig. S8), consistent with the ability of this CXCL12 variant to act as an agonist of ACKR3 (20). Additionally, $CXCL12_{P2G}$ also promoted formation of the active-like intermediate R*' conformation (R*' increased by 6%, Figs. 4D & E, Fig. S8), suggesting that activation of ACKR3 can be achieved by populating the R*' state, not just the R* state, which is consistent with a flexible, distortion activation mechanism. Together, $CXCL12_{P2G}$ increased active (R*) and active-like (R*') conformations by 11%, somewhat less than observed for $CXCL12_{WT}$ (24%, Fig. 2C, Fig. S8). $CXCL12_{LRHQ}$ also promoted the active (R*) and active-like (R*') conformations of ACKR3 (R* + R*' increased by 11%, Fig. 4F, Fig. S8). Additionally, the probabilities of R ↔ R' transitions were suppressed relative to apo receptor in the presence of $CXCL12_{P2G}$, while the probabilities for R'* ↔ R* transitions were enhanced in the presence of the $CXCL12_{LRHQ}$ (Figs. 4E & F). These differences may be a consequence of the longer residence time of the LRHQ mutant on the receptor (57). The agonism observed for both chemokine variants (19, 20) suggests that both the active R* and active-like R*' conformations of ACKR3 are sufficient for GRK phosphorylation and arrestin recruitment.

<u>ACKR3 constitutive activity is linked to receptor conformational heterogeneity.</u>
As noted above, apo-ACKR3 displays little conformational selectivity, with similar occupancies observed for all four FRET states (Fig. 2C). We hypothesized that this might be related to the constitutive activity of the receptor (13, 16) and tied to the presence of Tyr at position $257^{6.40}$ (Fig. 5A), which is a hydrophobic residue (V, I, or L) in all other chemokine receptors. In many other class A GPCRs, mutating the residue at 6.40 results in constitutive activity (32, 58-60) and previous analysis of rhodopsin suggests that this is a consequence of lowering the energy barrier for transitions between different receptor conformations (61). In our previous work, we showed that mutation of $Y257^{6.40}$ to leucine, the corresponding amino acid in CXCR4, reduces constitutive arrestin recruitment to ACKR3, while preserving the ability of the receptor to be activated by CXCL12 (Fig. S9) (16). Adding this single-point mutation to our ACKR3 smFRET construct had a significant impact, converting the broad conformational distribution of the WT apo-receptor to a narrower distribution concentrated in the high-FRET region (Figs. 5B & C). Overall, the FRET histogram is similar to what we observe for apo-CXCR4 (Fig. 2A), although the active conformation is still split between R* and R*' states (the latter unique to ACKR3) (Fig. 5C). State-to-state transitions were also suppressed relative to WT ACKR3 (Figs. 5B & C). This result indicates that $Y257^{6.40}$ is a major determinant of the broad conformational heterogeneity of ACKR3.

$CXCL12_{WT}$ promoted active and active-like conformations of $Y257^{6.40}L$ ACKR3 (R* + R*' increased by 16%, Figs. 5C & E), although the effect was somewhat reduced in comparison to WT ACKR3 (R* + R*' increased by 24%, Figs. 5B & D). Consistent with this, the mutant receptor recruits β-arrestin in response to $CXCL12_{WT}$ with an E_{max} value that is only slightly reduced relative to the WT receptor (Fig. S9, ~80% of WT) (16), suggesting again that the population of the R*' intermediate conformational state may contribute to receptor activation.

Discussion

The molecular basis for the atypical pharmacological behavior of ACKR3 is not well understood. Since structures of ACKR3 show intracellular loop disorder, and progressive structural substitutions within the loops fail to promote G protein coupling (16), we recently proposed that the atypical nature of ACKR3 may be related to receptor conformational dynamics (16, 62). Consistent with this hypothesis, in the present study we found that the conformational dynamics of ACKR3 and the canonical GPCR CXCR4 are indeed markedly different. Our smFRET results revealed four distinct conformations of apo-ACKR3 with approximately equal populations: inactive R, active R*, R' (inactive-like) and R*' (active-like) (Fig. 2C). The state-to-state TDP plots (Fig. 2C) further reinforced the notion that ACKR3 is a flexible receptor that readily exchanges between different conformational states, consistent with our previous structural studies where a flexible intracellular interface in the absence of interaction partners was observed (16). In contrast, apo-CXCR4 primarily populates the inactive R state, with only a single intermediate state (R'), and relatively few transitions between states (Fig. 2A). These observations imply that ACKR3 has a relatively flat energy landscape, with similar energy minima for the different conformations, whereas the energy landscape of CXCR4 is more rugged (Fig. 6). For both receptors, the energy barriers between states are sufficiently high that transitions occur relatively slowly with seconds long dwell times (Figs. 1C and S2).

The relatively flat energy landscape of ACKR3 may account for the propensity of ACKR3 to be activated by a diverse range of ligands. In principle, ligands could promote activation by providing more energetically favorable binding interactions with the receptor in the active R* or R*' conformations relative to the inactive R or R' conformations. Alternatively, ligands could destabilize the inactive R or R' conformations of the receptor, which would also shift the receptor population to the active conformation(s). Our results do not distinguish between these two possibilities. Regardless, the similar free energies of different receptor conformations in ACKR3 (Fig. 6) implies that relatively little energy is required to switch the receptor from one state to another. Moreover, activation can be achieved by populating either the R* or R*' state. Thus, independent of specific binding poses and receptor interactions, a variety of different ligands may be able to tip the balance between different receptor conformations.

The TDP plots demonstrate that the R' state in CXCR4 and the R' and R*' states in ACKR3 are intermediate species that lie on the pathway between inactive R and active R* receptor conformations. SmFRET studies of the glucagon receptor (39) and the $A2_{AR}$ (40) (both labeled in TM4 and TM6, as here) also revealed a discrete intermediate receptor conformation. In principle, the intermediates in CXCR4 and ACKR3 could represent partial movements of TM6 from the inactive to active conformation or more subtle conformational changes altering the photophysical characteristics of the probes without drastically altering the donor-acceptor distance. Either possibility leads to detectable changes in apparent FRET efficiency and reflect discrete conformational steps on the activation pathway; however, it is not possible to resolve specific structural changes from the data. Interestingly, the R*' intermediate appears to be unique to ACKR3. Moreover, this state responds to agonist and inverse agonist ligands in the same manner as the active R* state: agonists increase the population of the R*' state, while an inverse agonist decreases the population. In contrast, the single intermediate state in CXCR4 (R') is not responsive or only weakly responsive to ligands. The presence of both active (R*) and active-like (R*') conformations in ACKR3 may be responsible for its activation prone nature and ligand promiscuity.

Structural features that make ACKR3 conformationally flexible include Y257$^{6.40}$, which we previously showed contributes to the constitutive activity of ACKR3 (16). Similar to the constitutively active M257$^{6.40}$Y mutant of rhodopsin, Y$^{6.40}$ in ACKR3 stacks against Y$^{5.58}$ and Y$^{7.53}$ and stabilizes the active-like conformation (63). Additionally, the broad conformational distribution and high probability of state-to-state transitions of ACKR3 parallel the dramatically lower energy barrier of the M257$^{6.40}$Y rhodopsin mutant relative to WT rhodopsin (61). By contrast, mutation of Y257$^{6.40}$ to leucine, the corresponding amino acid in CXCR4, promoted the dominance of an inactive high-FRET receptor conformation similar to CXCR4 (Figs. 2A & 5C); it also reduced the transition probabilities (Figs. 5B & C) and the ability of ACKR3 to constitutively recruit arrestin (16).

In addition to the contribution of Y257$^{6.40}$ to the dynamic behavior of ACKR3, a disulfide bond between C34 in the receptor N-terminus and C287 in extracellular loop 3 (ECL3), observed in all other reported chemokine receptor-chemokine structures (64-66) is conspicuously missing in cryo-EM structures of ACKR3 with chemokine and small molecule agonists (16). Furthermore, ACKR3 remains functional in the absence of these cysteines (67) unlike other chemokine receptors (68, 69). The disulfide may constrain the relative positions of TM1 and TM6/7 and the opening of the orthosteric pocket; therefore, its absence may confer ACKR3 with greater conformational flexibility than other chemokine receptors, consistent with our observations. It may also allow ACKR3 to be activated by diverse ligands.

Our results provide insights into the linkage between receptor conformation and ligand pharmacology in CXCR4. The chemokine variants CXCL12$_{P2G}$ and CXCL12$_{LRHQ}$ are reported to act as antagonists of CXCR4 (19, 20), and the small molecule IT1t acts as an inverse agonist (54-56). Surprisingly, none of these ligands inhibit formation of the active R* conformation of CXCR4. In fact, the chemokine variants both stabilize and increase this state to some degree, although less effectively than CXCL12$_{WT}$. Thus, the antagonism and inverse agonism of these ligands does not appear to be linked exclusively to receptor conformation, suggesting that the ligands inhibit coupling of G proteins to CXCR4 or disrupt the ligand-receptor-G protein interaction network required for signaling (Fig. S10) (21, 23). Interestingly, these ligands also increase the probabilities of state-to-state transitions (Figs. 3B & 4B), suggesting that enhanced conformational exchange prevents the receptor from productively engaging G proteins. Similarly, ACKR3 is naturally dynamic and lacks G protein coupling, suggesting a common mechanism of G protein antagonism. Future smFRET studies performed in the presence of G proteins should be informative in this regard.

An unusual aspect of ACKR3 behavior is the failure to activate G proteins. Instead, ACKR3 recruits arrestins in response to phosphorylation of its C-terminal tail. Why ACKR3 does not couple to G proteins, at least in most cells, is unclear and not readily explained by differences in primary sequence, since insertion of a DRY box motif and substitution of all ICLs from a canonical GPCR failed to confer G protein activity (16). It is possible that the active receptor conformation clashes sterically with the G protein as suggested by docking of G proteins to structures of ACKR3 (16). Alternatively, the receptor dynamics and conformational transitions revealed here may prevent formation of productive contacts between ACKR3 and G protein that are required for coupling, even though G proteins appear to constitutively associate with the receptor (13, 16, 70). An important caveat is

that our study does not report on the dynamics of the other TM helices and H8, some of which are known to participate in arrestin interactions (31, 32). Lack of a well-organized intracellular pocket due to frequent conformational transitions may also explain why the fingerloop of arrestin is not observed to interact with the pocket, in contrast with other GPCRs (71, 72), but instead inserts into membranes/micelles adjacent to the receptor (62). Nevertheless, arrestins are still recruited to CXCL12-stimulated ACKR3 due to GRK phosphorylation of the receptor C-terminal tail (15, 73). Since GRKs also interact with the cytoplasmic pocket to facilitate phosphorylation, it remains to be determined how dynamics might decouple G protein activation and arrestin binding to the receptor cytoplasmic pocket (62) while supporting pocket-mediated GRK activity. However, given the fleeting interaction between GRKs and GPCRs (74), rapid state sampling by ACKR3 may not necessarily be detrimental to GRK engagement and phosphorylation. Furthermore, conformational intermediates in addition to the fully active receptor have been shown to be targets for GRK phosphorylation, such as the early photoactivated rhodopsin metarhodopsin I (75). A more constrained system may be necessary to promote productive interactions between ACKR3 and G proteins. Along these lines, a local increase of membrane pressure in certain cell environments could explain the apparent ability of ACKR3 to activate G proteins in astrocytes and glioma cells (12, 13). The atypical activation of ACKR3 does not appear to be dependent on any singular receptor feature and is likely a combination of several factors.

The pharmacological behavior of ACKR3 resembles the human cytomegalovirus chemokine receptor US28, which also recognizes diverse chemokines, constitutively internalizes, and displays multiple functional conformations (76). Similar to ACKR3, US28 appears to be activated by distortion of the orthosteric binding pocket rather than by specific side chain contacts between receptor and ligand, which is supported by multiple active conformations observed for both apo-US28 and US28 with different agonists (76-79). Whether US28 also has a relatively flat energy landscape like ACKR3 remains to be seen. The conformational dynamics and activation mechanisms revealed here for ACKR3 may also be operative in other chemokine receptors that respond to multiple ligands and have considerable constitutive activity, such as CCR1, CCR2, and CCR3 (64, 80). Finally, the ability of ACKR3 to be activated by populating more than one conformational state may explain why antagonizing the receptor by targeting the orthosteric binding pocket has proven to be challenging; in contrast, the specific requirements for CXCR4 agonism has permitted the development of many orthosteric antagonists but few agonists (81). Drug discovery efforts aimed at inhibiting ACKR3 may therefore require allosteric strategies.

Materials and Methods

Unless otherwise stated all chemicals and reagents were purchased from SigmaAldrich or Fisher Scientific. Methoxy e-Coelenterazine (Prolume Purple) was purchased from Nanolight Technologies (Prolume LTD).

Cloning

Human ACKR3 (residues 2-362) preceded by an N-terminal HA signal sequence and followed by C-terminal 10His and FLAG tags was cloned into the pFasBac vector for purification from *Sf9* cells. Human CXCR4 (residues 2-352) with an N-terminal FLAG tag and C-terminal 10His was inserted into pFasBac for purification. For cell-based assays, ACKR3 (residues 2-362) or CXCR4 (residues 2-352) were inserted into pcDNA3.1 expression vector with an N-terminal FLAG tag and followed with a C-terminal *Renilla*

491 luciferase II (ACKR3_rlucII and CXCR4_rlucII). Site-directed mutagenesis was performed
492 by overlap extension and confirmed by Sanger sequencing. No native cysteines were
493 substituted for either CXCR4 or ACKR3.
494
495 Arrestin recruitment by BRET
496 Arrestin recruitment to ACKR3 and CXCR4 was detected using a BRET2 assay as
497 previously described (15, 57). Briefly, HEK293T cells (ATCC) were plated at 750k/well in
498 a 6-well dish in Dulbecco's modified eagle media (DMEM) with 10% fetal bovine serum
499 (FBS) and transfected 24 hrs later with 50 ng receptor_rlucII DNA, 1 µg GFP10_β-
500 arrestin2 (a kind gift from N. Heveker, Université de Montréal, Canada), and 1.4 µg empty
501 pcDNA3.1 vector using TransIT-LT1 transfection system (MirusBio) and expressed for 40
502 hrs. The cells were then washed with PBS (137 mM NaCl, 2.7 mM KCl, 10 mM Na_2HPO_4,
503 1.8 mM KH_2PO_4, pH 7.4) and mechanically lifted in Tyrode's buffer (25 mM HEPES, 140
504 mM NaCl, 1 mM $CaCl_2$, 2.7 mM KCl, 12 mM $NaHCO_3$, 5.6 mM Glucose, 0.5 mM $MgCl_2$,
505 0.37 mM NaH_2PO_4, pH 7.5). 100k cells were plated per 96-well white BRET plate (BD
506 Fisher) and reattached for 45 min at 37 °C. GFP expression was checked using a
507 SpectraMax M5 plate fluorometer (Molecular Devices) with 485 nm excitation, 538 nm
508 emission, and 530 nm cutoff. 5 µM Prolume Purple substrate was subsequently added
509 and total luminescence detected using a TECAN Spark Luminometer (TECAN Life
510 Sciences) at 37 °C. CXCL12 was then added to each well at the indicated final
511 concentrations and BRET was read using default BRET2 settings (blue emission 360-440
512 nm, red emission 505-575 nm) and an integration time of 0.5 sec. Experiments were
513 baseline matched and normalized to the E_{max} of WT receptor. The reported data is the
514 average of three independent experiments performed in duplicate. Points were fit to a
515 sigmoidal dose-response model using SigmaPlot 11.0 (Systat Software, Inc).
516
517 Receptor purification, labeling, and nanodisc reconstitution
518 M159$^{4.40}$C/Q245$^{6.28}$C ACKR3 (WT and Y257$^{6.40}$L) and L150$^{4.40}$C/Q233$^{6.29}$C CXCR4 were
519 purified from *Sf9* cells (Expression Systems) as previously described (16). Briefly, *Sf9* cells
520 were infected with baculovirus (prepared using Bac-to-Bac Baculovirus Expression
521 System, Invitrogen) containing either the mutant ACKR3 or CXCR4. Cells were harvested
522 after 48 hrs and membranes dounce homogenized in hypotonic buffer (10 mM HEPES pH
523 7.5, 10 mM $MgCl_2$, 20 mM KCl) followed three more times with hypotonic buffer with 1 M
524 NaCl. The membranes were spun down at 50k x g for 30 min and resuspended between
525 each round of douncing. After the final round, membranes were incubated with 100 µM
526 CCX662 (Chemocentryx Inc.) for ACKR3 or 100 µM IT1t for CXCR4 and solubilized in 50
527 mM HEPES pH 7.5, 400 mM NaCl, 0.75/0.15% dodecyl maltoside/cholesteryl
528 hemisuccinate (DDM/CHS) with a protease inhibitor tablet (Roche) for 4 hrs. Insoluble
529 material was then removed by centrifugation at 50k x g for 30 min and Talon resin
530 (Clontech) with 20 mM imidazole overnight binding at 4 °C. The resin was then transferred
531 to a column and washed with WB1 (50 mM HEPES pH 7.5, 400 mM NaCl, 0.1/0.02%
532 DDM/CHS, 10% glycerol, 20 mM imidazole) followed by WB2 (WB1 with 0.025/0.005%
533 DDM/CHS) and finally eluted with WB2 with 250 mM imidazole. The imidazole was
534 removed by desalting column (PD MiniTrap G-25, GE Healthcare). Final protein
535 concentration was determined by A_{280} using an extinction coefficient of 75000 $M^{-1}cm^{-1}$
536 (ACKR3) and 58850 $M^{-1}cm^{-1}$ (CXCR4). Samples were snap frozen in liquid nitrogen, and
537 stored at -80 °C until use.
538

539 When ready to prepare samples for smFRET measurements, two nanomoles of receptor
540 was thawed and incubated with fourteen nanomoles of Alexa Fluor 555 C2 maleimide
541 (A555) and Cy5 maleimide overnight at 4 °C with rotation. The next morning, free label
542 was removed by dilution using a 100k Da cut-off spin concentrator (Amicon) and the
543 sample concentrated to ~100 µl. Label incorporation was evaluated by measuring the
544 absorbance at A_{280} (ε_{280} = 75000 $M^{-1}cm^{-1}$ for ACKR3 and 58850 $M^{-1}cm^{-1}$ for CXCR4), A_{555}
545 (ε_{555} = 150000 $M^{-1}cm^{-1}$), and A_{645} (ε_{645} = 250000 $M^{-1}cm^{-1}$) to detect the concentrations of
546 the labeled receptor, A555, and Cy5, respectively. The contribution of the fluorophores to
547 A_{280} was removed before determining labeled receptor concentration. The entire sample
548 was used for nanodisc reconstitution.
549
550 Labeled receptors were reconstituted into biotinylated MSP1E3D1 nanodiscs as
551 previously described (16). Briefly, 1-palmitoyl-2-oleoyl-*sn*-glycero-3-phosphocholine
552 (POPC, Avanti) and 1-palmitoyl-2-oleoyl-*sn*-glycero-3-phospho-(1'-rac-glycerol) (POPG,
553 Avanti) were prepared in a 3:2 POPC:POPG ratio and solubilized in ND buffer (25 mM
554 HEPES pH 7.5, 150 mM NaCl, 180 mM cholate). MSP1E3D1 was expressed and purified
555 as previously described (82) and biotinylated with EZ-Link NHS-polyethylene glycol 4
556 (PEG4)-Biotin (Thermo Fisher) per manufacturer instructions. The receptors, MSP1E3D1,
557 and lipids were combined at a molar ratio of 0.1:1:110 for ACKR3:MSP:lipids respectively.
558 Additional ND buffer was added to keep the final cholate concentration >20 mM. After 30
559 min at 4 °C, 200 mg of Biobeads (Bio-Rad) were added and incubated for 3-6 hrs. The
560 sample was then loaded on a Superdex 200 10/300 GL column equilibrated with 25 mM
561 HEPES pH 7.5, 150 mM NaCl and fractions containing nanodisc complexes were
562 combined. 200 µl Talon resin was added with 20 mM imidazole (final concentration) and
563 the samples were incubated for 16 hrs at 4 °C. The resin was then transferred to a Micro
564 Bio-Spin Column (Bio-Rad) and washed with 25 mM HEPES pH 7.5, 150 mM NaCl, 20
565 mM imidazole and eluted with 25 mM HEPES pH 7.5, 150 mM NaCl, 250 mM imidazole.
566 Imidazole was removed by buffer-exchange using 100k Da spin concentrators and 25 mM
567 HEPES pH 7.5, 150 mM NaCl. Sample were concentrated to ~1 µM and stored at 4 °C
568 until use.
569
570 <u>CXCL12 purification from *E. Coli*</u>
571 CXCL12 was expressed and purified as previously described (15, 16). Briefly, the
572 chemokines were expressed by IPTG induction in BL21(DE3)pLysS cells. The cells were
573 collected by centrifugation, resuspended in 50 mM tris pH 7.5, 150 mM NaCl and lysed by
574 sonication. Inclusion bodies were then collected by centrifugation, resuspended in
575 equilibration buffer (50 mM tris, 6 M guanidine-HCl pH 8.0), sonicated to release the
576 chemokines and the samples centrifuged again to pellet insoluble material. The
577 supernatant was then passed over a Ni-nitrilotriacetic acid (NTA) column equilibrated with
578 equilibration buffer to bind the His-tagged chemokines. The column was washed with
579 wash buffer (50 mM MES pH 6.0, 6 M guanidine-HCl) and eluted with 50 mM acetate pH
580 4.0, 6 M guanidine-HCl. The chemokine-containing elutions were pooled and dithiothreitol
581 (DTT) added to a final concentration of 4 mM. After incubating 10 min, the solution was
582 added dropwise into refolding buffer (50 mM tris pH 7.5, 500 mM arginine-HCl, 1 mM
583 EDTA, 1 mM oxidized glutathione) and incubated at room temperature for 4 hrs before
584 dialyzing against 20 mM tris pH 8.0, 50 mM NaCl. To remove the N-terminal purification
585 tag, enterokinase was added and the sample incubated at 37 °C for 5 days. Uncleaved
586 chemokine and free tags were removed by reverse Ni-NTA and eluted with wash buffer.
587 Finally, the sample was purified on a reverse-phase C18 column equilibrated with 75%

buffer A (0.1% trifluoroacetic acid (TFA)) and 25% buffer B (0.1% TFA, 90% acetonitrile) and eluted by a linear gradient of buffer B. The pure protein was lyophilized and stored at -80 °C until use.

smFRET microscopy

smFRET experiments were performed on a custom built prism-based TIRF microscope as previously described (83). Briefly, a flow cell was assembled on a quartz slide passivated with polyethylene glycol (PEG) and a small fraction of biotinylated PEG, after which neutravidin was introduced (84). Labeled ACKR3 or CXCR4 in biotinylated nanodiscs were diluted into trolox buffer (25 mM HEPES pH 7.5, 150 mM NaCl, 1 mM propyl gallate, 5 mM trolox), flowed into the sample chamber, and incubated for 5 min at room temperature. The samples were then washed twice with imaging buffer (trolox buffer with 2 mM protocatechuic acid, 50 nM protocatechuate-3,4-dioxygenase). Movies were collected with 100 ms integration time using a custom single-molecule data acquisition program to control the CCD camera (Andor). Single-molecule donor and acceptor emission traces were extracted from the recordings using custom IDL (Interactive Data Language) scripts. The software packages used to control the CCD camera and extract time trajectories were provided by Dr. Taekjip Ha. In all cases, five initial apo-receptor movies were recorded at different locations on the slide and then ligand was flowed into the cell by two washes with chemokine or small molecule in imaging buffer at final concentrations of 500 nM for chemokines ($CXCL12_{WT}$, $CXCL12_{P2G}$, $CXCL12_{LRHQ}$, CXCL11) and 1 μM for the small molecules (IT1t, VUF16840, VUF15485). Ten more movies were collected for each condition at different locations on the slide. The data presented are a composite of at least three individual slides and treatments.

FRET trajectories were generated and analyzed using custom software written in-house (https://github.com/rpauszek/smtirf). Donor and acceptor traces for each molecule were corrected for donor bleed through and background signal and apparent FRET efficiencies were calculated as $E_{app} = I_A/(I_A+I_D)$, where E_{app} is the apparent FRET efficiency at each time point and I_D and I_A are the corresponding donor and acceptor fluorophore intensities, respectively. Traces were screened manually for single donor and acceptor bleach steps and anti-correlated behavior between fluorophores to confirm the presence of single receptors within the identified particles and single donor and acceptor labeling. All traces for a particular protein/ligand combination were analyzed globally by a single Hidden Markov Model assuming two, three, four, or five states and shared variance as previously described (83). Briefly, each model was trained on all selected trajectories for a given sample simultaneously using an expectation-maximization method (85). Once a model was trained, the Viterbi algorithm (85) was used to determine the most likely hidden path for each trajectory. This labeled state path was then used to aggregate all data points belonging to a particular state in order to compile composite histograms of apparent FRET efficiency, using a Kernel Density estimation algorithm (Python package Scikit-learn, version 1.2.2) with a Gaussian kernel and a bandwidth of 0.04. The relative populations of distinct FRET states were directly obtained during compilation of the corresponding histograms. The resulting apparent FRET efficiency histograms were fit with a Gaussian Mixture Model (Scikit-learn) and the corresponding Bayesian Information Criterion (BIC) was calculated as described (86). Transition density probability plots revealing the connectivity among individual FRET states were calculated as described (87).

Data availability

All relevant data supporting this study are included in the Article or Supplementary files and are available from the authors upon request.

Acknowledgments

We gratefully acknowledge the initial work on this project undertaken by Chunxia Zhao and Rajan Lamichhane. Additionally, we thank Handel lab members Cheyanne Shinn, Catherina Salanga, and Nicholas Chimileski for providing the chemokines CXCL11 and $CXCL12_{P2G}$, respectively, R. Leurs (Vrije Universiteit Amsterdam) for the small molecules VUF16840 and VUF15485, and N. Heveker (Université de Montréal) for the GFP10_β-arrestin2 plasmid. This work was supported by National Institutes of Health grants R01 GM133157 (D.P.M./T.M.H), R01 CA254402 (T.M.H.), R01 AI161880 (T.M.H.), F32 GM137505 (C.T.S.), F32 GM115017 (R.F.P.) and T32 AI007354 (R.F.P.). Additional support was from the Robertson Foundation/Cancer Research Institute Irvington Postdoctoral Fellowship (M.G.).

Author Contributions:

Conception and design of the research: C.T.S., T.M.H., and D.P.M.
Methodology: C.T.S., R.F.P., and M.G.
Software: R.F.P.
Validation: C.T.S. and R.F.P.
Formal Analysis: C.T.S. and R.F.P.
Investigation: C.T.S.
Writing-Original Draft Preparation: C.T.S., T.M.H., and D.P.M.
Writing-Reviewing & Editing: C.T.S., R.F.P., M.G., T.M.H., and D.P.M.
Visualization: C.T.S. and R.F.P.
Supervision: T.M.H. and D.P.M.
Funding Acquisition: T.M.H. and D.P.M.

Competing Interest Statement: T.M.H. is a cofounder of Lassogen Inc. and serves on the Scientific Advisory Boards of Abilita Bio, and Abalone Bio. The terms of these arrangements have been reviewed and approved by the University of California, San Diego in accordance with its conflict of interest policies. The other authors declare that they have no competing interests.

References

1. S. Chatterjee, B. Behnam Azad, S. Nimmagadda, The intricate role of CXCR4 in cancer. *Adv Cancer Res* **124**, 31-82 (2014).
2. F. Balkwill, The significance of cancer cell expression of the chemokine receptor CXCR4. *Semin Cancer Biol* **14**, 171-179 (2004).
3. U. M. Domanska *et al.*, A review on CXCR4/CXCL12 axis in oncology: no place to hide. *Eur J Cancer* **49**, 219-230 (2013).
4. N. Kawaguchi, T. T. Zhang, T. Nakanishi, Involvement of CXCR4 in Normal and Abnormal Development. *Cells* **8**, 185 (2019).
5. I. Kufareva, M. Gustavsson, Y. Zheng, B. S. Stephens, T. M. Handel, What Do Structures Tell Us About Chemokine Receptor Function and Antagonism? *Annu Rev Biophys* **46**, 175-198 (2017).
6. J. W. Griffith, C. L. Sokol, A. D. Luster, Chemokines and chemokine receptors: positioning cells for host defense and immunity. *Annu Rev Immunol* **32**, 659-702 (2014).

686 7. R. J. Nibbs, G. J. Graham, Immune regulation by atypical chemokine receptors.
687 *Nat Rev Immunol* **13**, 815-829 (2013).
688 8. A. Vacchini, M. Locati, E. M. Borroni, Overview and potential unifying themes of
689 the atypical chemokine receptor family. *J Leukoc Biol* **99**, 883-892 (2016).
690 9. F. Saaber *et al.*, ACKR3 Regulation of Neuronal Migration Requires ACKR3
691 Phosphorylation, but Not beta-Arrestin. *Cell Rep* **26**, 1473-1488.e1479 (2019).
692 10. S. Lau *et al.*, A negative-feedback loop maintains optimal chemokine
693 concentrations for directional cell migration. *Nat Cell Biol* **22**, 266-273 (2020).
694 11. M. Wong *et al.*, Dynamic Buffering of Extracellular Chemokine by a Dedicated
695 Scavenger Pathway Enables Robust Adaptation during Directed Tissue
696 Migration. *Dev Cell* **52**, 492-508 e410 (2020).
697 12. V. Odemis *et al.*, The presumed atypical chemokine receptor CXCR7 signals
698 through G(i/o) proteins in primary rodent astrocytes and human glioma cells. *Glia*
699 **60**, 372-381 (2012).
700 13. A. Fumagalli *et al.*, The atypical chemokine receptor 3 interacts with Connexin 43
701 inhibiting astrocytic gap junctional intercellular communication. *Nat Commun* **11**,
702 4855 (2020).
703 14. S. Rajagopal *et al.*, Beta-arrestin- but not G protein-mediated signaling by the
704 "decoy" receptor CXCR7. *Proc Natl Acad Sci U S A* **107**, 628-632 (2010).
705 15. C. T. Schafer, Q. Chen, J. J. G. Tesmer, T. M. Handel, Atypical Chemokine
706 Receptor 3 'Senses' CXC Chemokine Receptor 4 Activation Through GPCR
707 Kinase Phosphorylation. *Mol Pharmacol* **104**, 174-186 (2023).
708 16. Y. C. Yen *et al.*, Structures of atypical chemokine receptor 3 reveal the basis for
709 its promiscuity and signaling bias. *Sci Adv* **8**, eabn8063 (2022).
710 17. B. E. Hopkins *et al.*, Effects of Small Molecule Ligands on ACKR3 Receptors.
711 *Mol Pharmacol* **102**, 128-138 (2022).
712 18. U. Naumann *et al.*, CXCR7 functions as a scavenger for CXCL12 and CXCL11.
713 *PLoS One* **5**, e9175 (2010).
714 19. M. S. Hanes *et al.*, Dual targeting of the chemokine receptors CXCR4 and
715 ACKR3 with novel engineered chemokines. *J Biol Chem* **290**, 22385-22397
716 (2015).
717 20. A. Jaracz-Ros *et al.*, Differential activity and selectivity of N-terminal modified
718 CXCL12 chemokines at the CXCR4 and ACKR3 receptors. *J Leukoc Biol* **107**,
719 1123-1135 (2020).
720 21. T. Ngo *et al.*, Crosslinking-guided geometry of a complete CXC receptor-
721 chemokine complex and the basis of chemokine subfamily selectivity. *PLoS Biol*
722 **18**, e3000656 (2020).
723 22. M. P. Wescott *et al.*, Signal transmission through the CXC chemokine receptor 4
724 (CXCR4) transmembrane helices. *Proc Natl Acad Sci U S A* **113**, 9928-9933
725 (2016).
726 23. B. S. Stephens, T. Ngo, I. Kufareva, T. M. Handel, Functional anatomy of the full-
727 length CXCR4-CXCL12 complex systematically dissected by quantitative model-
728 guided mutagenesis. *Sci Signal* **13**, eaay5024 (2020).
729 24. Y. Liu *et al.*, Cryo-EM structure of monomeric CXCL12-bound CXCR4 in the
730 active state. *Cell Rep* **43**, 114578 (2024).
731 25. K. Saotome *et al.*, Structural insights into CXCR4 modulation and
732 oligomerization. *Nat Struct Mol Biol* 10.1038/s41594-024-01397-1 (2024).

733 26. J. M. Burns *et al.*, A novel chemokine receptor for SDF-1 and I-TAC involved in
734 cell survival, cell adhesion, and tumor development. *J Exp Med* **203**, 2201-2213
735 (2006).
736 27. K. R. Klein *et al.*, Decoy receptor CXCR7 modulates adrenomedullin-mediated
737 cardiac and lymphatic vascular development. *Dev Cell* **30**, 528-540 (2014).
738 28. Y. Ikeda, H. Kumagai, A. Skach, M. Sato, M. Yanagisawa, Modulation of
739 circadian glucocorticoid oscillation via adrenal opioid-CXCR7 signaling alters
740 emotional behavior. *Cell* **155**, 1323-1336 (2013).
741 29. M. Meyrath *et al.*, The atypical chemokine receptor ACKR3/CXCR7 is a broad-
742 spectrum scavenger for opioid peptides. *Nat Commun* **11**, 3033 (2020).
743 30. J. J. Liu, R. Horst, V. Katritch, R. C. Stevens, K. Wuthrich, Biased signaling
744 pathways in beta2-adrenergic receptor characterized by 19F-NMR. *Science* **335**,
745 1106-1110 (2012).
746 31. L. M. Wingler *et al.*, Angiotensin Analogs with Divergent Bias Stabilize Distinct
747 Receptor Conformations. *Cell* **176**, 468-478 e411 (2019).
748 32. J. F. Fay, D. L. Farrens, Structural dynamics and energetics underlying allosteric
749 inactivation of the cannabinoid receptor CB1. *Proc Natl Acad Sci U S A* **112**,
750 8469-8474 (2015).
751 33. X. Yao *et al.*, Coupling ligand structure to specific conformational switches in the
752 beta2-adrenoceptor. *Nat Chem Biol* **2**, 417-422 (2006).
753 34. M. Elgeti, W. L. Hubbell, DEER Analysis of GPCR Conformational Heterogeneity.
754 *Biomolecules* **11**, 778 (2021).
755 35. L. M. Wingler *et al.*, Angiotensin and biased analogs induce structurally distinct
756 active conformations within a GPCR. *Science* **367**, 888-892 (2020).
757 36. A. P. Ray, N. Thakur, N. G. Pour, M. T. Eddy, Dual mechanisms of cholesterol-
758 GPCR interactions that depend on membrane phospholipid composition.
759 *Structure* **31**, 836-847 e836 (2023).
760 37. C. T. Schafer, J. F. Fay, J. M. Janz, D. L. Farrens, Decay of an active GPCR:
761 Conformational dynamics govern agonist rebinding and persistence of an active,
762 yet empty, receptor state. *Proc Natl Acad Sci U S A* **113**, 11961-11966 (2016).
763 38. G. G. Gregorio *et al.*, Single-molecule analysis of ligand efficacy in beta(2)AR-G-
764 protein activation. *Nature* **547**, 68-73 (2017).
765 39. K. Krishna Kumar *et al.*, Negative allosteric modulation of the glucagon receptor
766 by RAMP2. *Cell* **186**, 1465-1477 e1418 (2023).
767 40. D. D. Fernandes *et al.*, Ligand modulation of the conformational dynamics of the
768 A(2A) adenosine receptor revealed by single-molecule fluorescence. *Sci Rep* **11**,
769 5910 (2021).
770 41. I. G. Denisov, S. G. Sligar, Nanodiscs for structural and functional studies of
771 membrane proteins. *Nat Struct Mol Biol* **23**, 481-486 (2016).
772 42. I. G. Denisov, S. G. Sligar, Nanodiscs in Membrane Biochemistry and
773 Biophysics. *Chem Rev* **117**, 4669-4713 (2017).
774 43. S. A. Eberle, M. Gustavsson, Bilayer lipids modulate ligand binding to atypical
775 chemokine receptor 3. *Structure* **32**, 1174-1183 e1175 (2024).
776 44. H. Tsukamoto, A. Sinha, M. DeWitt, D. L. Farrens, Monomeric rhodopsin is the
777 minimal functional unit required for arrestin binding. *J Mol Biol* **399**, 501-511
778 (2010).
779 45. S. A. Eberle, M. Gustavsson, A Scintillation Proximity Assay for Real-Time
780 Kinetic Analysis of Chemokine-Chemokine Receptor Interactions. *Cells* **11**, 1317
781 (2022).

46. S. G. Rasmussen *et al.*, Crystal structure of the beta2 adrenergic receptor-Gs protein complex. *Nature* **477**, 549-555 (2011).
47. J. Zhao *et al.*, Ligand efficacy modulates conformational dynamics of the micro-opioid receptor. *Nature* **629**, 474-480 (2024).
48. K. Palczewski *et al.*, Crystal structure of rhodopsin: A G protein-coupled receptor. *Science* **289**, 739-745 (2000).
49. S. G. Rasmussen *et al.*, Crystal structure of the human beta2 adrenergic G-protein-coupled receptor. *Nature* **450**, 383-387 (2007).
50. D. L. Farrens, C. Altenbach, K. Yang, W. L. Hubbell, H. G. Khorana, Requirement of rigid-body motion of transmembrane helices for light activation of rhodopsin. *Science* **274**, 768-770 (1996).
51. A. B. Kleist *et al.*, Conformational selection guides beta-arrestin recruitment at a biased G protein-coupled receptor. *Science* **377**, 222-228 (2022).
52. O. Otun *et al.*, Conformational dynamics underlying atypical chemokine receptor 3 activation. *Proc Natl Acad Sci U S A* **121**, e2404000121 (2024).
53. C. Perpina-Viciano *et al.*, Kinetic Analysis of the Early Signaling Steps of the Human Chemokine Receptor CXCR4. *Mol Pharmacol* **98**, 72-87 (2020).
54. C. E. Mona *et al.*, Design, synthesis, and biological evaluation of CXCR4 ligands. *Org Biomol Chem* **14**, 10298-10311 (2016).
55. E. M. Rosenberg, Jr. *et al.*, Characterization, Dynamics, and Mechanism of CXCR4 Antagonists on a Constitutively Active Mutant. *Cell Chem Biol* **26**, 662-673 e667 (2019).
56. A. Zarca *et al.*, Pharmacological characterization and radiolabeling of VUF15485, a high-affinity small-molecule agonist for the atypical chemokine receptor ACKR3. *Mol Pharmacol* **105**, 301-312 (2024).
57. M. Gustavsson, D. P. Dyer, C. Zhao, T. M. Handel, Kinetics of CXCL12 binding to atypical chemokine receptor 3 reveal a role for the receptor N terminus in chemokine binding. *Sci Signal* **12**, eaaw3657 (2019).
58. M. Han, S. O. Smith, T. P. Sakmar, Constitutive activation of opsin by mutation of methionine 257 on transmembrane helix 6. *Biochemistry* **37**, 8253-8261 (1998).
59. X. Han, S. D. Tachado, H. Koziel, W. A. Boisvert, Leu128(3.43) (I128) and Val247(6.40) (V247) of CXCR1 are critical amino acid residues for g protein coupling and receptor activation. *PLoS One* **7**, e42765 (2012).
60. M. Cui *et al.*, Crystal structure of a constitutive active mutant of adenosine A(2A) receptor. *IUCrJ* **9**, 333-341 (2022).
61. H. Tsukamoto, D. L. Farrens, A constitutively activating mutation alters the dynamics and energetics of a key conformational change in a ligand-free G protein-coupled receptor. *J Biol Chem* **288**, 28207-28216 (2013).
62. Q. Chen *et al.*, ACKR3-arrestin2/3 complexes reveal molecular consequences of GRK-dependent barcoding. *bioRxiv* 10.1101/2023.07.18.549504 (2023).
63. X. Deupi *et al.*, Stabilized G protein binding site in the structure of constitutively active metarhodopsin-II. *Proc Natl Acad Sci U S A* **109**, 119-124 (2012).
64. Z. Shao *et al.*, Molecular insights into ligand recognition and activation of chemokine receptors CCR2 and CCR3. *Cell Discov* **8**, 44 (2022).
65. L. Qin *et al.*, Structural biology. Crystal structure of the chemokine receptor CXCR4 in complex with a viral chemokine. *Science* **347**, 1117-1122 (2015).
66. K. Liu *et al.*, Structural basis of CXC chemokine receptor 2 activation and signalling. *Nature* **585**, 135-140 (2020).

830 67. M. Szpakowska *et al.*, Mutational analysis of the extracellular disulphide bridges
831 of the atypical chemokine receptor ACKR3/CXCR7 uncovers multiple binding
832 and activation modes for its chemokine and endogenous non-chemokine
833 agonists. *Biochem Pharmacol* **153**, 299-309 (2018).
834 68. L. S. Ai, F. Liao, Mutating the four extracellular cysteines in the chemokine
835 receptor CCR6 reveals their differing roles in receptor trafficking, ligand binding,
836 and signaling. *Biochemistry* **41**, 8332-8341 (2002).
837 69. C. Limatola *et al.*, Cysteine residues are critical for chemokine receptor CXCR2
838 functional properties. *Exp Cell Res* **307**, 65-75 (2005).
839 70. A. Levoye, K. Balabanian, F. Baleux, F. Bachelerie, B. Lagane, CXCR7
840 heterodimerizes with CXCR4 and regulates CXCL12-mediated G protein
841 signaling. *Blood* **113**, 6085-6093 (2009).
842 71. D. P. Staus *et al.*, Structure of the M2 muscarinic receptor-beta-arrestin complex
843 in a lipid nanodisc. *Nature* **579**, 297-302 (2020).
844 72. W. Huang *et al.*, Structure of the neurotensin receptor 1 in complex with beta-
845 arrestin 1. *Nature* **579**, 303-308 (2020).
846 73. P. Sarma *et al.*, Molecular insights into intrinsic transducer-coupling bias in the
847 CXCR4-CXCR7 system. *Nat Commun* **14**, 4808 (2023).
848 74. A. Pulvermuller, K. Palczewski, K. P. Hofmann, Interaction between
849 photoactivated rhodopsin and its kinase: stability and kinetics of complex
850 formation. *Biochemistry* **32**, 14082-14088 (1993).
851 75. R. Paulsen, J. Bentrop, Activation of rhodopsin phosphorylation is triggered by
852 the lumirhodopsin-metarhodopsin I transition. *Nature* **302**, 417-419 (1983).
853 76. T. W. M. De Groof *et al.*, Selective targeting of ligand-dependent and -
854 independent signaling by GPCR conformation-specific anti-US28 intrabodies. *Nat*
855 *Commun* **12**, 4357 (2021).
856 77. J. S. Burg *et al.*, Structural biology. Structural basis for chemokine recognition
857 and activation of a viral G protein-coupled receptor. *Science* **347**, 1113-1117
858 (2015).
859 78. T. F. Miles *et al.*, Viral GPCR US28 can signal in response to chemokine
860 agonists of nearly unlimited structural degeneracy. *Elife* **7** (2018).
861 79. N. Tsutsumi *et al.*, Atypical structural snapshots of human cytomegalovirus
862 GPCR interactions with host G proteins. *Sci Adv* **8**, eabl5442 (2022).
863 80. C. T. Gilliland, C. L. Salanga, T. Kawamura, J. Trejo, T. M. Handel, The
864 chemokine receptor CCR1 is constitutively active, which leads to G protein-
865 independent, beta-arrestin-mediated internalization. *J Biol Chem* **288**, 32194-
866 32210 (2013).
867 81. M. Lefrancois *et al.*, Agonists for the Chemokine Receptor CXCR4. *ACS Med*
868 *Chem Lett* **2**, 597-602 (2011).
869 82. T. K. Ritchie *et al.*, Chapter 11 - Reconstitution of membrane proteins in
870 phospholipid bilayer nanodiscs. *Methods Enzymol* **464**, 211-231 (2009).
871 83. R. F. Pauszek, 3rd, R. Lamichhane, A. Rajkarnikar Singh, D. P. Millar, Single-
872 molecule view of coordination in a multi-functional DNA polymerase. *Elife* **10**
873 (2021).
874 84. R. Lamichhane, A. Solem, W. Black, D. Rueda, Single-molecule FRET of protein-
875 nucleic acid and protein-protein complexes: surface passivation and
876 immobilization. *Methods* **52**, 192-200 (2010).
877 85. L. R. Rabiner, A Tutorial on Hidden Markov-Models and Selected Applications in
878 Speech Recognition. *P Ieee* **77**, 257-286 (1989).

879 86. G. Schwarz, Estimating the Dimension of a Model. *Ann. Statist.* **6**, 461-464
880 (1978).
881 87. S. A. McKinney, C. Joo, T. Ha, Analysis of single-molecule FRET trajectories
882 using hidden Markov modeling. *Biophys J* **91**, 1941-1951 (2006).

883
884

Figures and Tables

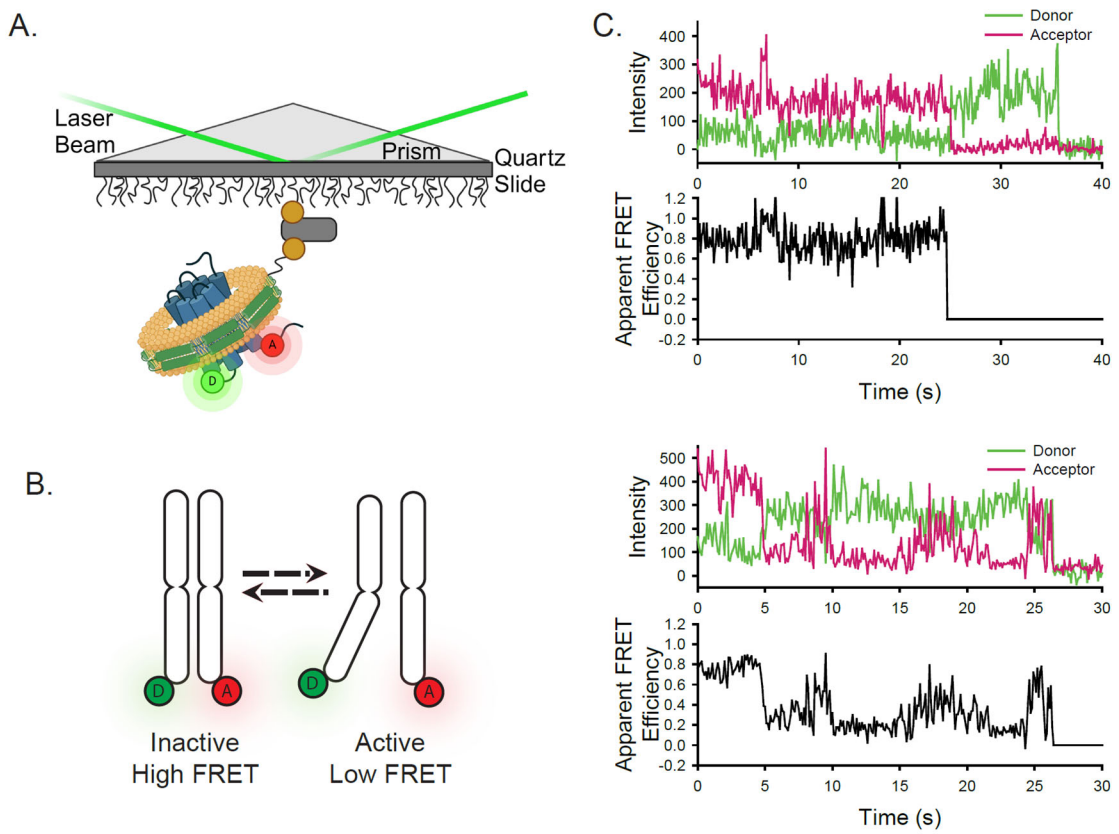

Figure 1. Experimental design of the smFRET system. A) A single receptor molecule (blue) was labeled with donor (D) and acceptor (A) fluorophores, inserted into a phospholipid (yellow) nanodisc (green), and immobilized on a quartz slide via biotin (tan circle)-neutravidin (grey rectangle) attachment. A prism facilitates total internal reflection of the excitation laser to excite only donor fluorophores close to the surface. B) Cartoon depicting inactive (left) and active (right) receptor conformations. C) Two representative single-molecule time traces for apo-ACKR3. In both examples, the donor (green) and acceptor (red) intensities are shown in the top panel and the corresponding apparent FRET efficiency (black) is shown in the bottom panel.

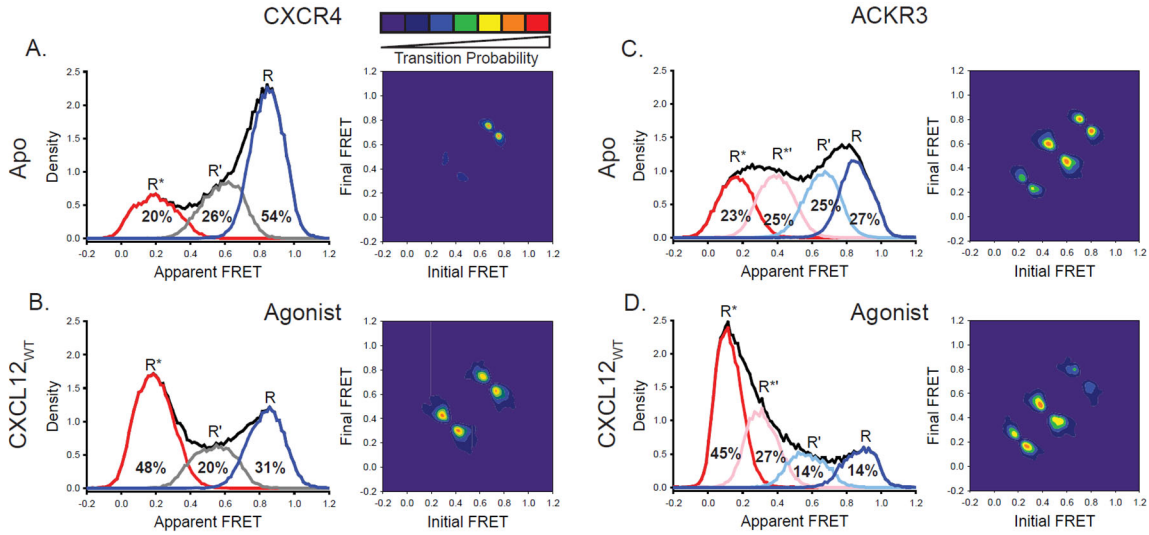

Figure 2. ACKR3 exhibits greater conformational flexibility compared to CXCR4. A) Apparent FRET efficiency histogram of apo-CXCR4 (left, black trace) resolved into three distinct conformational states: a high-FRET state corresponding to the inactive receptor conformation (R, blue), a low-FRET active receptor conformation (R*, red) and an intermediate conformation (R', gray). The fractional populations of each state obtained from global analysis are indicated. The receptor is mostly in the inactive conformation. A transition density probability (TDP) plot (right) displays the relative probabilities of transitions from an initial FRET state (x-axis) to a final FRET state (y-axis). For apo-CXCR4, transitions between R and R' states are observed most frequently. B) Addition of $CXCL12_{WT}$ to CXCR4 shifted the conformational distribution to the low-FRET R* state and resulted in more transitions between all three FRET states. C) The broad apparent FRET efficiency histogram of apo-ACKR3 (left, black trace) is resolved into four distinct conformational states: inactive R (blue), active R* (red), inactive-like R' (light blue), and active-like R*' (pink). Little conformational preference is observed among these states. Moreover, all possible sequential state-to-state transitions are observed (right). D) Addition of $CXCL12_{WT}$ to ACKR3 shifted the conformational distribution to the low-FRET R* state, which was also reflected in the transition probabilities. In all cases, data sets represent the analysis of at least three independent experiments.

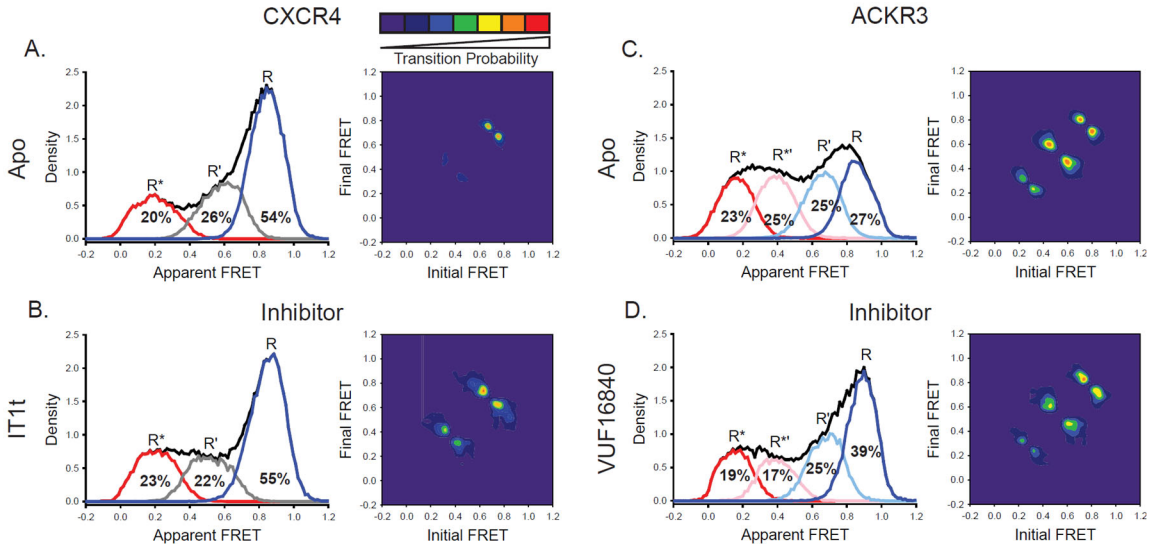

Figure 3. A small molecule inhibitor shifts the ACKR3 conformational population to the inactive FRET state, while CXCR4 is largely unaffected. A) FRET distributions and TDP of apo-CXCR4 repeated from Fig. 2A for comparison. B) Treatment of CXCR4 with the inhibitor IT1t had little impact on the FRET distribution, but increased transition probabilities compared to the apo-receptor. C) FRET distributions and TDP of apo-ACKR3 repeated from Fig. 2C for comparison. D) Treatment of ACKR3 with VUF16480, an inverse agonist, shifted the conformational distribution and TDP to the high-FRET inactive R conformation. Data sets represent the analysis of at least three independent experiments. The overall apparent FRET efficiency envelopes for the samples are represented by the black traces.

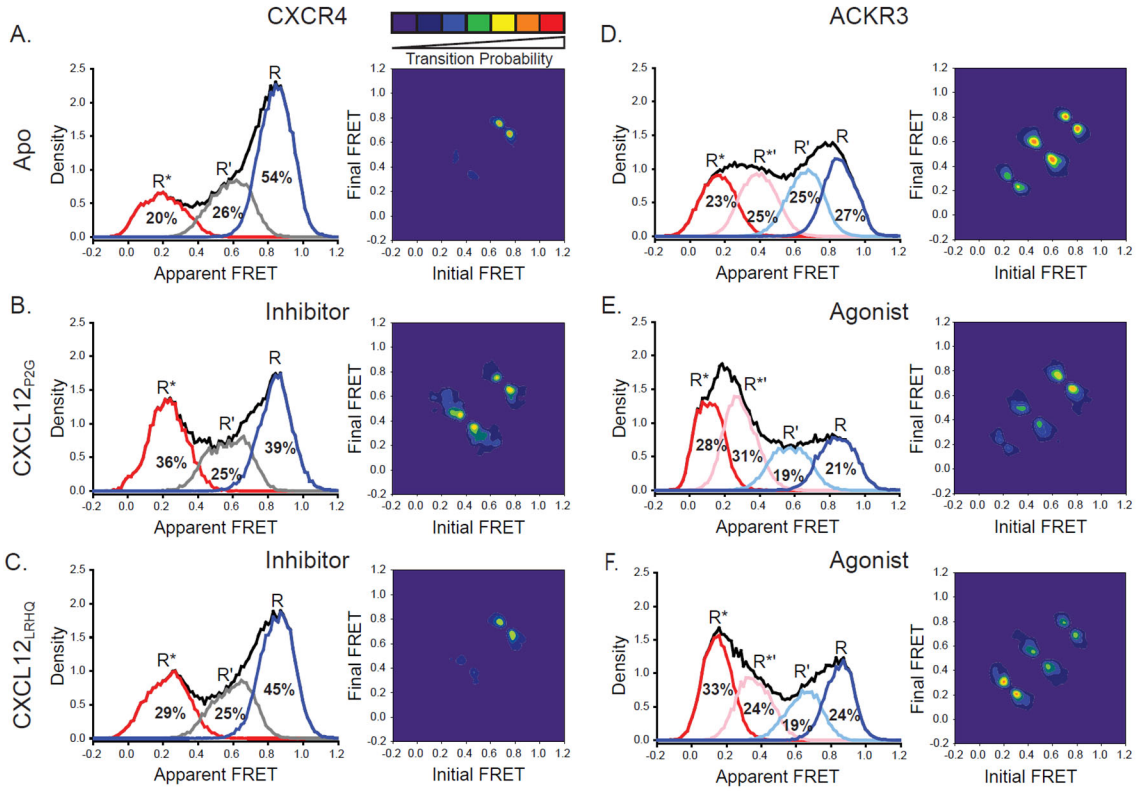

Figure 4. CXCL12 variants containing mutations to the N-terminus promoted active receptor conformations in both CXCR4 and ACKR3. A) FRET distributions and TDP for apo-CXCR4 repeated from Fig. 2A for reference. B) Addition of $CXCL12_{P2G}$ to CXCR4 promoted a shift to the low-FRET active (R*) conformation and an increase in state-to-state transition probabilities. C) $CXCL12_{LRHQ}$ led to a more subtle shift to the R* conformation of CXCR4 without affecting the transition probabilities. D) FRET distributions and TDP for apo-ACKR3 repeated from Fig. 2C. E) Treatment of ACKR3 with $CXCL12_{P2G}$ displayed a shift to low-FRET, R*' and R* states, while reducing the transition probabilities for R' ↔ R*' and R*' ↔ R* transitions relative to the apo-receptor. F) $CXCL12_{LRHQ}$ treatment of ACKR3 shifted the FRET distribution to the low-FRET R* active state and promoted R*' ↔ R* transitions relative to the apo-receptor. In all cases, the data sets represent the analysis of at least three independent experiments. The overall apparent FRET efficiency envelopes for the samples are represented by the black traces.

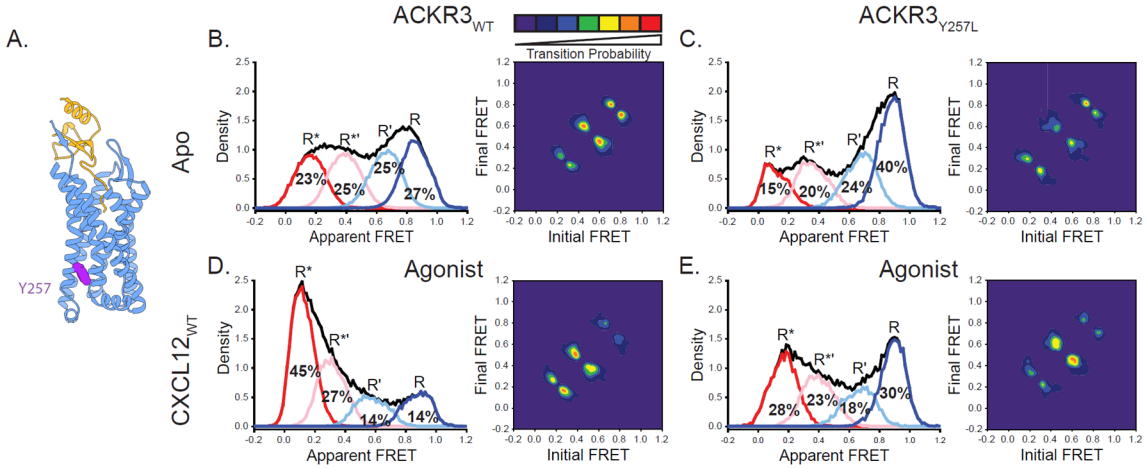

Figure 5. Replacement of Y257$^{6.40}$ with the corresponding residue in CXCR4 (leucine) reduces conformational heterogeneity of ACKR3. A) Structure of ACKR3 bound with CXCL12$_{WT}$ (PDBID: 7SK3) highlighting the location of Y257$^{6.40}$ (purple) (16). B) Apparent FRET efficiency distributions and TDP of WT ACKR3 in the apo-state, repeated from Fig. 2C. C) The mutation Y257$^{6.40}$L shifted the conformational landscape of the apo-receptor to the high-FRET inactive R conformation at the expense of active R* and active-like R*' conformations, and also reduced the probability of state-to-state transitions. D) Apparent FRET efficiency distributions and TDP of WT ACKR3 treated with CXCL12$_{WT}$, repeated from Fig. 2D. E) Treatment of Y257$^{6.40}$L ACKR3 with CXCL12$_{WT}$ promoted more low-FRET active R* and active-like R*' states. Data sets represent the analysis of at least three independent experiments. The overall apparent FRET efficiency envelopes for the samples are represented by the black traces.

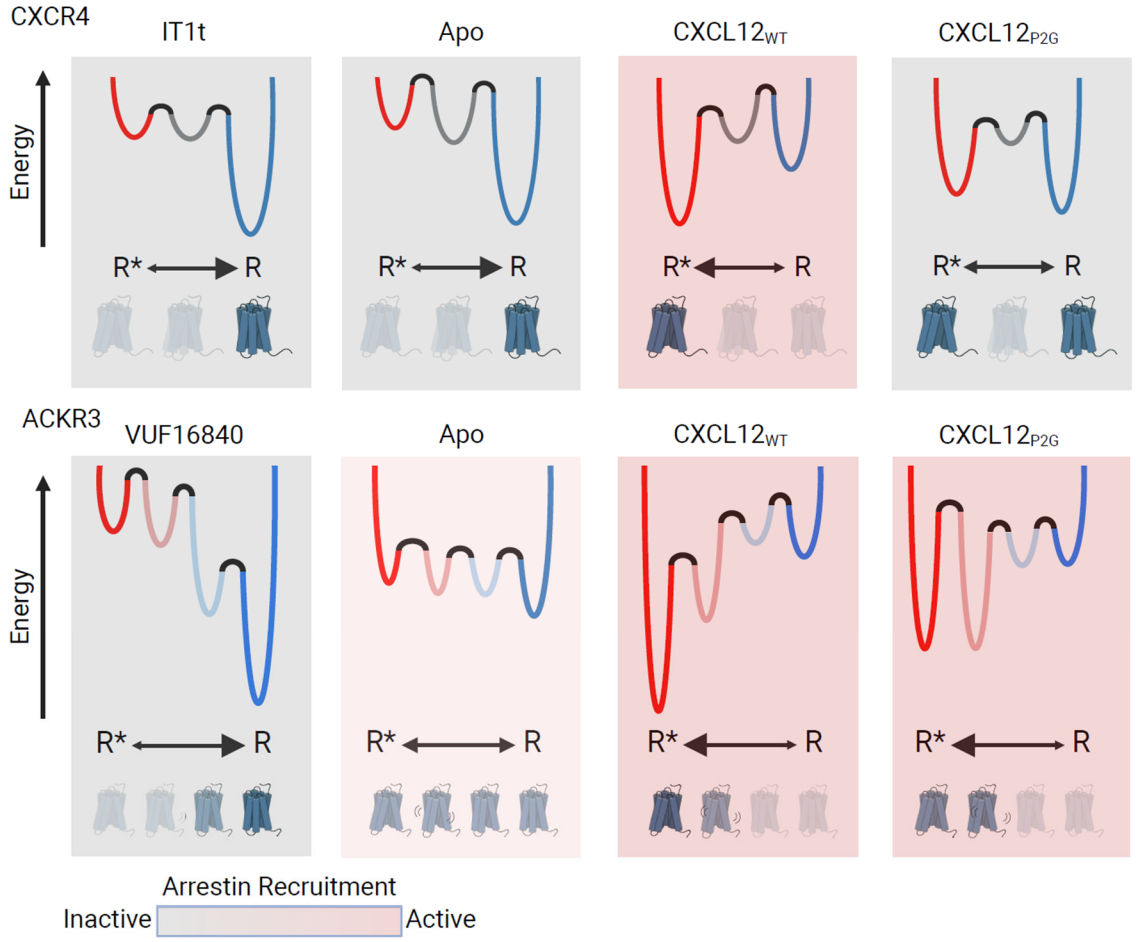

Figure 6. Schematic illustration of the conformational energy landscapes for CXCR4 and ACKR3, highlighting the differences in the responsiveness of the two receptors to ligands. CXCR4 populates three distinct conformations, shown here as wells on the energy landscape. Apo-CXCR4 is predominantly in the inactive R state. The receptor is converted incompletely to R* with $CXCL12_{WT}$ treatment, while the small molecule inhibitor IT1t has little impact on the conformational distribution. Though $CXCL12_{P2G}$ is an antagonist of CXCR4, the ligand promoted a detectable shift to the active R* state, suggesting TM6 movement is not sufficient for CXCR4 activation. In contrast, ACKR3 populates four distinct conformations and shows little preference among them in the apo-form. The inverse agonist, VUF16840, shifts the population to the inactive R conformation, while the agonists $CXCL12_{WT}$ and $CXCL12_{P2G}$ promote the R* and R*' populations of ACKR3. Despite stabilizing different levels of the active R* state and active-like intermediate R*' state, both $CXCL12_{WT}$ and $CXCL12_{P2G}$ are agonists of ACKR3. The flexibility of ACKR3 may contribute to the ligand-promiscuity of this atypical receptor. Figure created with biorender.com